## SCIENCE CHINA

# **Technological Sciences**



RESEARCH PAPER •

Special Topic: Water-Related Vision

January 2025, Vol. 68, Iss. 1, 1100402:1–1100402:8 https://doi.org/10.1007/s11431-024-2741-0

# Establishment and verification of theoretical model for underwater light-sheet Scheimpflug LiDAR system

Fei FENG<sup>1,2</sup>, Guojun WU<sup>1,2\*</sup>, Bo LIU<sup>1</sup>, Xu ZHAO<sup>1,2</sup>, Yafeng WU<sup>1</sup> & Jinghan XU<sup>1,2</sup>

<sup>1</sup> Xi'an Institute of Optics and Precision Mechanics, Chinese Academy of Sciences, Xi'an 710119, China
<sup>2</sup> University of Chinese Academy of Sciences, Beijing 100049, China

Received April 29, 2024; accepted July 3, 2024; published online December 31, 2024

Abstract The Scheimpflug imaging in the air can increase the depth-of-view and has been well studied with an accurate Scheimpflug imaging model. However, there is no corresponding underwater light-sheet Scheimpflug (ULSS) imaging model. As a result, imaging accuracy cannot be ensured in the design phase, which mainly relies on the post-calibration. In this paper, the ULSS imaging model is firstly established, which gives the relationship between the pixel number and target distance, as well as that between the target distance and range resolution. A new experimental bracket and an underwater Scheimflug imaging lens were designed and developed. Based on this new device, several experiments were carried out in a pool to study the range resolution of this ULSS LiDAR, by which the correctness of the imaging model was verified. It also shows that the newly designed ULSS LiDAR can achieve a millimeter-level resolution within 8 m.

Keywords underwater optical detection, 3D detection, range resolution, Scheimpflug imaging, LiDAR

Citation: Feng F, Wu G J, Liu B, et al. Establishment and verification of theoretical model for underwater light-sheet Scheimpflug LiDAR system. Sci China Tech Sci, 2025, 68(1): 1100402, https://doi.org/10.1007/s11431-024-2741-0

#### 1 Introduction

Underwater optical imaging technology has been widely used in seabed target monitoring, marine resources exploration [1], seabed topography surveys, underwater rescue, marine biology, and many other aspects [2]. It effectively supplements underwater acoustic detection technology, as underwater optical imaging has higher spatial resolution and a more intuitive imaging effect than sonar detection technology [3]. However, when light travels underwater, it will be strongly absorbed and scattered by water, which limits the imaging distance and resolution of underwater optical imaging [4].

Due to the wavelength selectivity of light absorption in water, illumination light sources with a wavelength of around 532 nm are typically chosen for underwater optical imaging since these lasers can travel farther underwater [5]. Active lighting technology can alleviate the impact of light

absorption on the imaging range, but it brings scattering aggravation. The scattering, especially backscatter, will reduce the signal-to-noise ratio of underwater optical imaging. In general, there are mainly three kinds of technologies used to reduce the impact of backscattering and achieve longdistance underwater 3D imaging: (1) underwater range-gated technology [6–8]; (2) underwater synchronous laser line scan (LLS) technology [9–12]; (3) light-sheet combined with long baseline technology (LLB) [13,14]. Underwater range-gated technology requires a larger volume and power consumption. The underwater three-dimensional imaging laser sensor developed by Imaki has a size of 25 cm in diameter, 60 cm in length, and the most extended detection range of 20 m. The sensor's transmitter was a 532-nm pulsed laser with a peak power of 5 kW, pulse width of 1 ns, and repetition rate of 50 kHz, the volume and power consumption are enormous [15]. Range-gated technology uses gate time to filter out backscatter. If the gating time is too long, the backscatter filtering effect will be affected. The width of the gate directly limits the depth-of-view in range-gated imaging, making it

<sup>\*</sup> Corresponding author (email: wuguojun@opt.ac.cn)

impossible to achieve large depth-of-view detection. The synchronous LLS imaging technology does not apply to detecting underwater large-range targets or large depth difference terrain. When the detection distance changes from 5.2 to 9.2 m, the lateral displacement of the imaging spot reaches 2.5 mm, much larger than the width of the linear sensor [16]. The first two technologies are unsuitable for carrying by small and medium-sized underwater carrier platforms, such as unmanned underwater vehicles (UUVs) and autonomous underwater vehicles (AUVs), to realize the large depth-of-view and high-precision underwater three-dimensional optical detection. The LLB technology utilizes the Scheimpflug principle to achieve a large depth-of-view, triangulation to achieve two-dimensional measurement, and a long baseline to reduce water scattering [17,18].

The Scheimpflug principle indicates that if the object plane, image plane, and lens plane intersect are in a straight line, all points on the object plane can be clearly imaged on the image plane [19]. Inspired by this principle, the onedimensional (1D) Scheimpflug LiDAR was developed [20]. The Scheimpflug LiDAR can image laser lines entering the atmosphere onto a tilted camera, and the image of the laser lines on the camera is distributed in a straight line. Different positions on the straight line represent different distances [20]. The 1D Scheimpflug LiDAR is widely used in fields such as atmospheric aerosol remote sensing [21–24], industrial combustion process observation [25], and aquatic ecosystem analysis [26]. Mei and Brydegaard [27] proved the feasibility of a novel concept of differential absorption LiDAR based on the Scheimpflug principle. Zhang et al. [28] proposed an optical measurement technique based on the Scheimpflug principle, which provides the possibility for measuring the small angle backscatter intensity of marine water bodies. However, they did not perform scattering angle correction when extracting backscatter intensity values. Liu et al. [29] developed a water-body Scheimpflug LiDAR and measured the dynamic attenuation coefficient of the waterbody by the LiDAR system. They addressed the refractive effect at the interface of air-glass water and modified the pixel distance relationship during water measurement. A two-dimensional (2D) Scheimpflug LiDAR system for 3D profiling of opaque objects in air was introduced in ref. [30]. An overwater light-sheet Scheimpflug LiDAR system with the addition of a digital camera for underwater 3D profiling was presented in ref. [31]. Lyu et al. [32] proposed a Hadamard single-pixel imaging based visible region location method to reduce the measurement time. Wang et al. [33] proposed an underwater structured light vision calibration method considering unknown refractive index. Xu et al. [34] proposed a novel reconstruction method based on multi-refraction to remedy the nonlinear refraction. Li et al. [35] proposed a high-accuracy refraction-considered and installation-error-independent calibration method for the underwater one-mirror galvanometric line-laser scanner.

The Scheimpflug LiDAR systems described above all are operated in the air. Even if the method in ref. [31] can detect the underwater target, it can only correct the measurement deviation caused by the refraction of the air-water interface, while the LiDAR system is still located above the water surface, making it unsuitable for deep-sea target detection. In this work, we introduce an underwater light-sheet Scheimpflug (ULSS) LiDAR system in which both the system and the detected target are all underwater. We established its imaging model, verified the accuracy of the model from both theoretical and experimental aspects, and researched its range resolution for underwater target detection.

### 2 Principles and methods

The principle of Scheimpflug imaging in air is shown in Figure 1(a), where the dashed line AA' represents the lens optical axis and BB' represents the marginal ray. AA'' is the reverse extension line of AA', and BA'' is the perpendicular line of AA'. B'C is the perpendicular line of AA'. AO represents the object distance I, and OA' represents the lens focal length f'. AB is the object detection depth relative to the reference plane, which is represented by y. A'B' is the image height, which is represented by x. By using  $\Delta OA''B$  and  $\Delta OCB'$  as similar triangles, the expression for the relative depth of object AB, which is represented by y, can be obtained as

$$y = \frac{-lx\sin\varphi}{f'\sin\theta - x\sin(\theta - \varphi)}.$$
 (1)

In eq. (1),  $\varphi$  is the Scheimpflug angle between the optical axis of the underwater imaging lens and the camera image plane.  $\theta$  is the angle between the optical axis of the underwater imaging lens and the laser beam. l is the optical axis objective distance. f' is the focal length of the underwater imaging lens.

The principle of Scheimpflug imaging in water is shown in Figure 1(b). Due to the different refractive indices of the object and image media, the marginal ray deviates in the image space relative to the object space, resulting in  $\Delta OA''B$  and  $\Delta OCB'$  not being similar. Therefore, the Scheimpflug eq. (1) in the air is unapplicable for ULSS imaging, and it is necessary to derive a formula specifically for ULSS imaging.

The marginal ray is deflected according to Snell's law in the water Scheimpflug imaging. The incident angle  $\angle BOA$ , represented by i, and the refraction angle  $\angle B'OC$ , defined by i', have the following relationship [36]:

$$n\sin i = n'\sin i'$$
. (2)

When the measurement plane is below the reference plane, from the right triangle  $\triangle OA''B$  and right triangle  $\triangle OB'C$  in

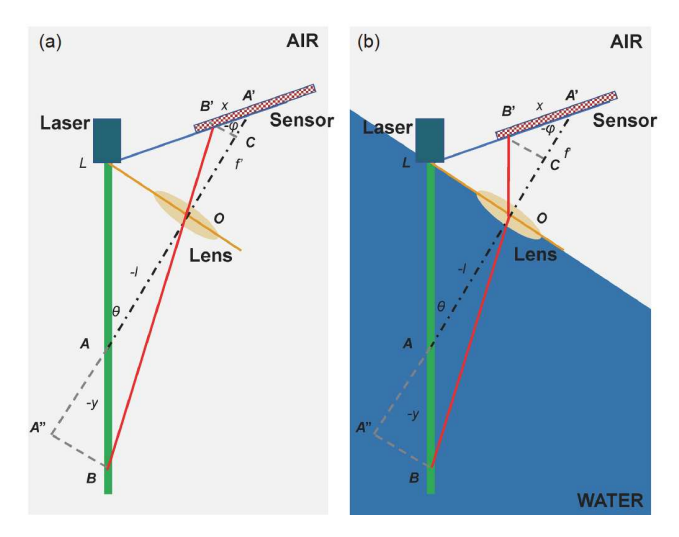


Figure 1 (Color online) Schematic diagram of the Scheimpflug principle when the measurement plane is below the reference plane (a) Scheimpflug principle in air. (b) Scheimpflug principle in water (When light or a plane is rotated at an acute angle to the optical axis, the angle formed by clockwise rotation is positive, and the angle formed by anticlockwise rotation is negative. Object height and image height are positive above and negative below the optical axis. The object distance and focal length are defined by the lens's negative left and positive right sides. According to the definition in Figure 1, the y, l, and  $\varphi$  are negative, the f' and x are positive). The dotted black line represents the lens axis; the red line represents the edge field-of-view light; the green line represents the laser plane or object plane; the brown line represents the lens plane; the blue line represents the image plane.

Figure 1(b), the expressions of sini and sini can be obtained respectively as follows:

$$\sin i = \frac{A''B}{OB} = \frac{-y\sin\theta}{\sqrt{y^2 + l^2 + 2yl\cos\theta}},\tag{3}$$

$$\sin i' = \frac{B'C}{OB'} = \frac{-x\sin\varphi}{\sqrt{x^2 + f'^2 - 2xf'\cos\varphi}}.$$
 (4)

Then we bring eqs. (3) and (4) to eq. (2), which yields the following expression:

$$\begin{cases}
\left(\frac{l}{y}\right)^{2} + 2\frac{l}{y}\cos\theta + \left[1 - \left(\frac{nOB'\sin\theta}{n'x\sin\varphi}\right)^{2}\right] = 0, \\
OB' = \sqrt{x^{2} + f'^{2} - 2xf'\cos\varphi}.
\end{cases} \tag{5}$$

By solving the above quadratic equation, the expression for l/y can be obtained as

$$\frac{1}{y} = -\cos\theta \pm \sin\theta \sqrt{\left(\frac{nOB'}{n'x\sin\varphi}\right)^2 - 1} \,. \tag{6}$$

 $\theta$  is less than 90°, and l/y is taken as positive values. Therefore, the positive and negative signs in the above equation are positive. After organizing and deforming the above equation, the expression for y can be obtained as follows:

$$\begin{cases} y = \frac{-lx\sin\varphi}{x\cos\theta\sin\varphi + \sin\theta\sqrt{\left(\frac{n}{n'}\right)^2 OB^{2} - (x\sin\varphi)^2}}, \\ OB' = \sqrt{x^2 + f'^2 - 2xf'\cos\varphi}. \end{cases}$$
(7)

Eq. (7) is the expression for the relationship between the object's depth and the image's height in ULSS imaging, respectively. The Scheimpflug imaging eq. (1) in air is a special form when n = n' = 1 in eq. (7). Because when n = n' = 1, there is the following relationship:

$$\sqrt{\left(\frac{n}{n'}\right)^2 OB'^2 - (x\sin\varphi)^2} = \sqrt{OB'^2 - B'C^2} = OC$$

$$= f' - x\cos\varphi. \tag{8}$$

The range resolution of ULSS LiDAR is expressed as the depth value of the object space corresponding to each pixel on the camera. It can be obtained by taking the derivative of eq. (7):

$$\Delta y = y' \Delta x. \tag{9}$$

#### 3 Experiment

A ULSS LiDAR experiment was designed to verify the theoretical analysis's correctness. The experimental system used an experimental bracket instead of an underwater transport platform, as shown in Figure 2, which consists of an experimental bracket, laser, camera, industrial computer, and counterweight. The bracket is made into an isosceles trapezoidal structure, and counterweights are installed in symmetrical positions to ensure that the entire experimental system remains balanced and stable in air and water. Meanwhile, the bracket is 6.8 m long and 1 m high, equipped with adapter clamps, and can be used to fix and install emission, receiving, and control systems.

The emission system consists of a laser and a laser-shaping lens. The laser is a commercial 532 nm continuous laser (5 W maximum output power), customized by Changchun New Industries Optoelectronics Tech. Co., Ltd. A Powell lens shapes the emitted laser and emits divergent sheet light with a divergence angle of 15° in length and 0.06° in width. The laser is encapsulated in a titanium alloy pressure-resistant seal housing, and the laser beam is emitted from the sapphire optical window at the front end of the pressure-resistant shell. The laser beam is perpendicular to the lower crossbeam of the bracket, while the plane of the light-sheet is perpendicular to the plane of the bracket.

The receiving system consists of an imaging lens and a low-light camera. The imaging lens is a specialized Scheimpflug objective designed and processed by us for ULSS imaging, in which the field of view angle is 41.7°,

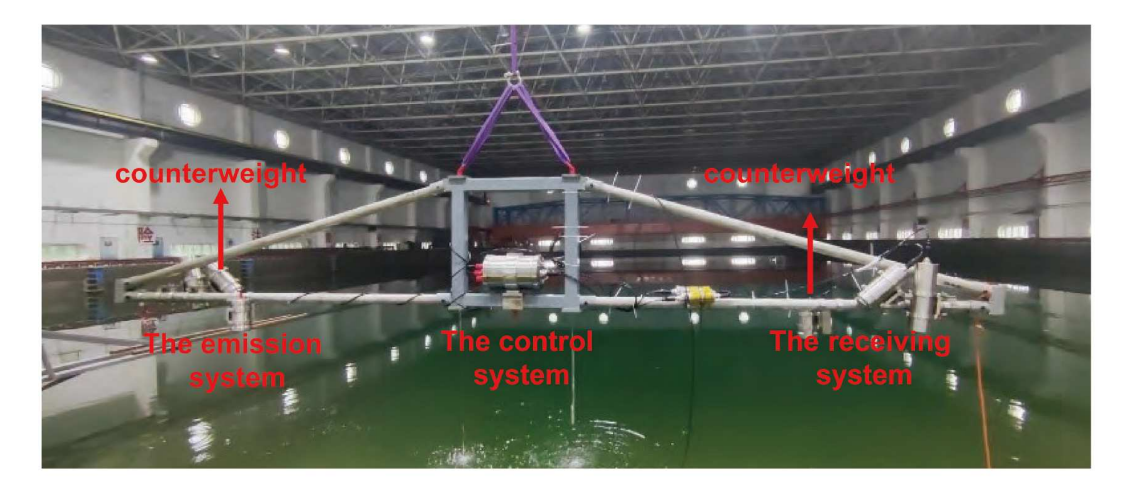


Figure 2 (Color online) Physical diagram of the underwater light LiDAR experimental device, including the experimental bracket, transmission system, receiving system, control system, and counterweight. The experimental bracket is a symmetrical structure, with the transmitting system and receiving system installed on both sides of the experimental bracket. Counterweights are seated at symmetrical positions to ensure the balance and stability of the experimental bracket in air and underwater. The experimental bracket and control system casing in the figure are only temporary structures used in the water tank experiment and are not components of the actual system. When the actual system is installed on the UUV, there will be no need for experimental brackets and control system casings. The circuit board in the control system will be dismantled and installed inside the UUV. Therefore, in practical applications, there are only three parts: the transmitting system, the control circuit board, and the receiving system. The volumes of these three parts are  $\emptyset$  149.99 mm  $\times$  256.10 mm, 69.89 mm  $\times$  176.10 mm  $\times$  58.34 mm, and  $\emptyset$  149.97 mm  $\times$  349.19 mm, respectively.

with a focal length of 22.87 mm. The low light camera adopts a commercial backlit Cmso, model HS-95-U3, produced by Fuzhou Indigo Imaging Technology Co., Ltd. The size of the photosensitive chip is 2 inches (2048 pixels  $\times$  2048 pixels, 11  $\mu m \times 11~\mu m$  pixel size, quantum efficiency 94.5% @ 570 nm). The camera and lens are packaged in titanium alloy pressure-resistant housing, which can withstand a pressure of 4000 m underwater.

The control system comprises a micro-industrial computer and a control circuit. It is completely sealed in a pressure-resistant housing. It can control laser output, adjust camera shooting parameters, and save captured images. The control system is installed in the middle of the experimental bracket to maintain the balance of the experimental bracket.

The focal length of the system is determined based on the field of view angle and the size of the camera chip. The project requires a field of view angle of  $2\omega \geqslant 40^{\circ}$ , which is to ensure sufficient scanning efficiency. The focal length can be determined by the following equation:

$$f' = \frac{n'Hp}{2n\tan(\omega_H)}. (10)$$

According to eq. (10), the relationship between the system field of view angle and the system focal length can be obtained. Using our proposed theoretical model, the relationship between the distance resolution at the farthest detection distance of 8.1 m and the lens focal length can be calculated. Two curves are plotted in one graph as shown in Figure 3.

From Figure 3, it can be found that the field of view angle decreases with the increase of focal length. The project requires a field of view angle greater than 40°, so the focal

length of the lens should be less than 23.1 mm. The larger the focal length, the higher the distance resolution (the smaller the distance that a single pixel can distinguish). To achieve the highest resolution, the focal length of the lens should be as large as possible. Based on the relationship between the comprehensive field of view angle, resolution, and focal length, the system focal length should be smaller than 23.1 mm, and the larger the better. Leave a certain margin for the field of view angle. In actual design, the focal length is 22.87 mm and the field of view angle is 41.7°.

Using our proposed theoretical model, when the focal length is 22.87 mm, the center field of view distance is 4.24 m, and the HS-95-U3 camera is used, the relationship

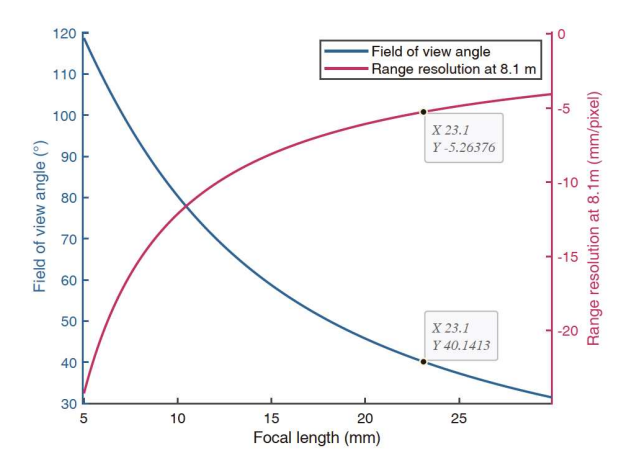


**Figure 3** (Color online) Relationship between focal length, field of view angle, and distance resolution (when the baseline length is 4800 mm, the angle x between the lens axis and the laser line is  $48.57^{\circ}$ , and the HS-95-U3 camera is used).

between the distance resolution at 8.1 m and the baseline length is shown in Figure 4.

From Figure 4, it can be found that the longer the baseline, the higher the distance resolution (the smaller the distance that a single pixel can distinguish). Due to the length limitation of the UUV used in the project, the system has chosen a baseline length of 4800 mm, which is the maximum available baseline length for the UUV.

The mutual relationship between the emission and receiving systems is shown in Figure 5. The baseline distance D between the camera and the laser is 4.8 m. The angle  $\theta$  between the optical axis of the imaging lens and the laser line

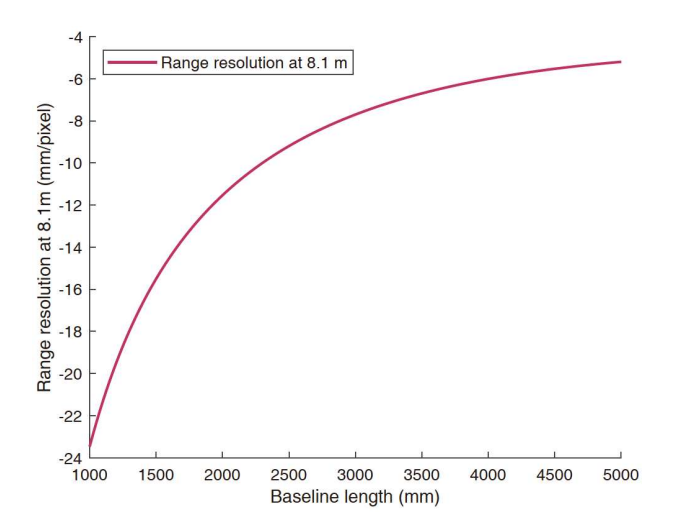


**Figure 4** (Color online) Relationship between distance resolution at 8.1 m and baseline length (when the focal length is 22.87 mm, the center field of view distance is 4.24 m, and the HS-95-U3 camera is used).

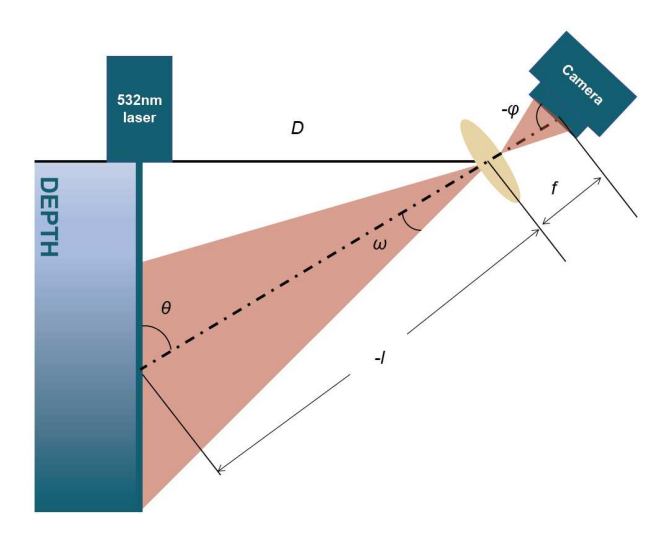


Figure 5 (Color online) Relative position relationship between the emission and receiving systems. D represents the baseline distance, and l represents the center field of view object distance. f represents the imaging lens focal length.  $H_{\min}$  and  $H_{\max}$  represent the nearest and farthest detection distances, respectively;  $\theta$  represents the angle between the laser beam and the optical axis of the imaging lens.  $\omega$  represents the field of view angle of the imaging lens.  $\varphi$  represents the angle of Scheimpflug.

is 48.57°. The imaging lens underwater field of view angle  $2\omega$  is 41.7°. The focal length f of the imaging lens is 22.87 mm. The Scheimpflug angle  $\varphi$  is 89.82°.

We use a tower-shaped cooperative target with a step height of 50 mm to measure the range accuracy of the ULSS LiDAR system. The tower-shaped cooperative target is shown in Figure 6(a). We sink the cooperative target into the bottom of the pool. The water in the pool is tap water with a refractive index of 1.3346. Then we lift the experimental bracket with a bridge crane, tie anti-oscillation ropes at both ends, and control the bracket's position and height so that the emission system's laser can shine on the cooperative target. The experimental process is shown in Figure 6(b). The bridge crane is used to control the distance between the experimental bracket and the cooperative target. Due to the cooperation target of having a 50 mm high staircase, laser lines on different steps are imaged at different pixel positions on the camera. The positions vary with the distance between the experimental bracket and the cooperative target.

#### 4 Results and discussion

We collected 12 underwater surface stripe images of targets at distances of 2.6, 3.1, 3.5, 3.95, 4.5, 5, 5.5, 6, 6.5, 6.9, 7.4, and 7.9 m, respectively. The captured image is shown in Figure 7. Based on the experimental parameters and theoretical model described in the previous chapters, we can obtain the theoretical relationship between pixel position and target distance, as shown by the red curve in Figure 8. In Figure 8, we calculated that the detection range of our ULSS LiDAR is 1.9–8.1 m.

According to eq. (7), the theoretical relationship function between pixel position and target distance can be calculated under the experimental parameters. The cooperative target of the experiment is to have three steps, and each image at different distances will have three line segments, each representing the height of one step. Through reading the pixel positions of the line segments in Figure 5, the results are

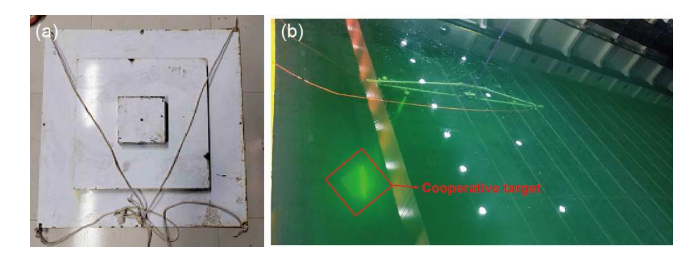


**Figure 6** (Color online) Experimental arrangement for range detection accuracy of ULSS LiDAR. (a) Cooperative target, step height 50 mm. (b) Sink the cooperative target into the bottom of the pool, use a bridge crane to control the distance between the experimental bracket and the cooperative target, and capture laser lines on the surface of the cooperative target at different distances. The experiment was conducted in a pool.

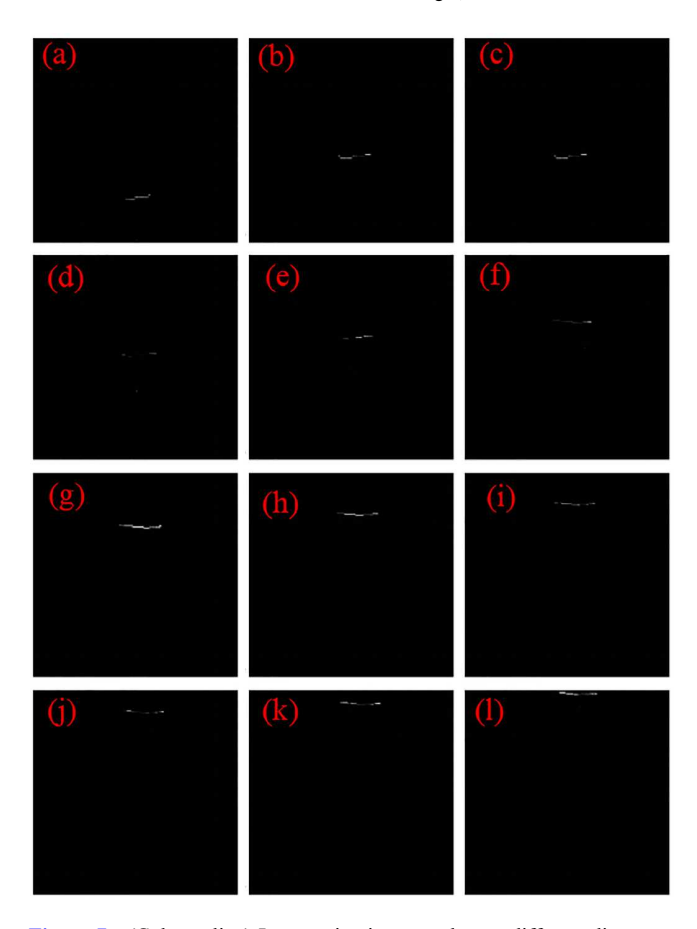


**Figure 7** (Color online) Laser stripe images taken at different distances. In the figure, (a)–(l) correspond to 2.6, 3.1, 3.5, 3.95, 4.5, 5, 5.5, 6, 6.5, 6.9, 7.4, and 7.9 m, respectively. The visible target distance is different, and the pixel positions in the image are different. Moreover, for the same step height, the number of pixels occupied by the step height varies depending on the distance.

#### shown in Table 1.

Figure 8 shows that the underwater optical imaging model

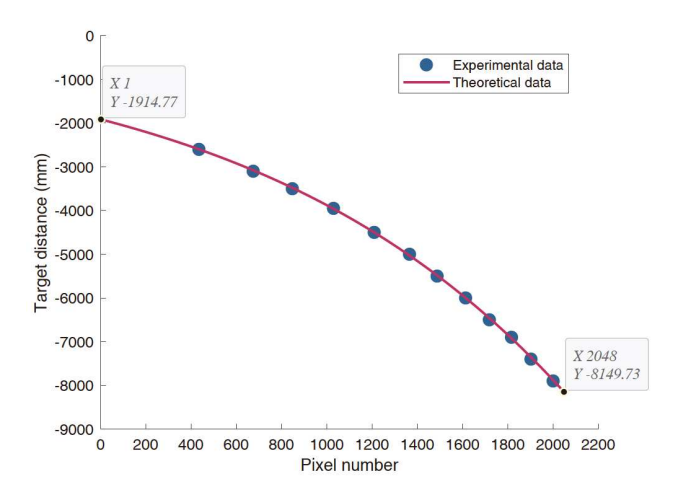


Figure 8 (Color online) Interrelationship between pixel number and target distance. The red solid line is the relationship curve between the number of pixels and the distance calculated according to the theoretical model, and the blue spots are the distribution of the number of pixels and the distance from the target in the actual image taken in the experiment. It can be found that the experimental data and the theoretical calculation curve are completely consistent, which verifies the correctness of the ULSS LiDAR detection model.

of the ULSS LiDAR we established is consistent with the experimental data, verifying the correctness of the theoretical model.

Because of the inability to provide continuously variable cooperative targets with precise heights, we used a tower-shaped target with a step height of 50 mm as the precision measurement cooperative target in the experiment. The definition of resolution is the object space distance corresponding to each pixel. In the experiment, cooperative target steps with different distances were collected, and each 50 mm step occupied a certain number of pixels in the image. Then, the object space distance corresponding to each pixel

Table 1 Experimental shooting of target distance and laser line pixel position results

Distances (mm)	Pixel number for step 1	Pixel number for step 2	Pixel number for step 3	Pixel number between steps 1 and 2	Pixel number between steps 2 and 3	Average pixel number	The distance corresponding to each pixel (mm)
-2600	434	456	477	23	22	22.5	-2.22
-3100	674	694	713	21	20	20.5	-2.44
-3500	847	864	881	18	18	18	-2.78
-3950	1029	1045	1059	17	15	16	-3.13
-4500	1209	1222	1235	14	14	14	-3.57
-5000	1365	1379	1392	15	14	14.5	-3.45
-5500	1487	1500	1512	14	13	13.5	-3.70
-6000	1613	1624	1636	12	13	12.5	-4.00
-6500	1718	1728	1739	11	12	11.5	-4.35
-6900	1816	1826	1835	11	10	10.5	-4.76
-7400	1902	1911	1920	9	10	9.5	-5.26
-7900	2000	2008	2016	9	9	9	-5.56

was calculated, which is the distance resolution. The calculation results are shown in the last column of Table 1. According to eq. (9), the theoretical resolution at different target distances can be calculated. The experimental data and theoretical resolution curve are plotted on the same data graph, as shown in Figure 9. It shows that the experimental data are basically consistent with the theoretical model, which verifies the correctness of the distance accuracy calculation model of ULSS LiDAR. It indicates that the underwater sheet light Scheimpflug LiDAR can achieve millimeter-level distance resolution within 8 m.

According to the refractive index data in the paper [37], it can be found that the maximum variation range of seawater refractive index is 1.33445–1.34507 when seawater temperature is between 0 and 30°C and salinity varies between 0‰–33‰. When the refractive index reaches the maximum and minimum extreme values, the relationship between pixel position and distance, as well as the relationship between distance and range resolution, are shown in Figures 10 and 11. It can be found that the change in refractive index has a relatively small impact on distance and range resolution.

#### 5 Conclusion

In this paper, a theoretical model for the ULSS LiDAR is proposed, based on which the relationship among the range resolution, the target distance, and other system parameters was derived. With the help of this model, a large depth-of-

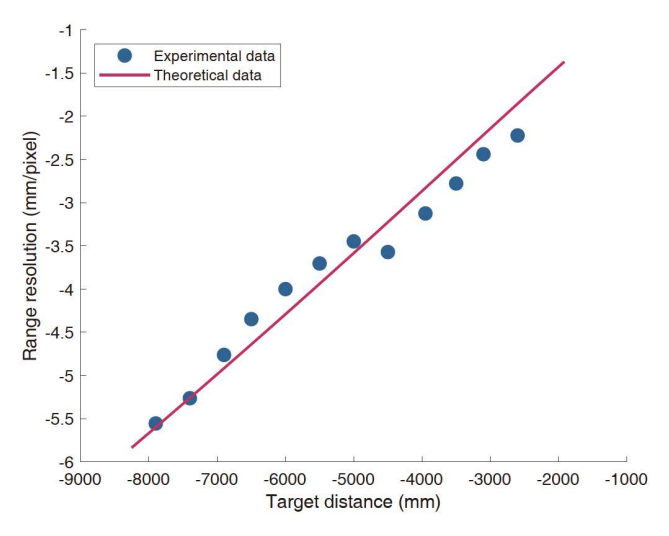
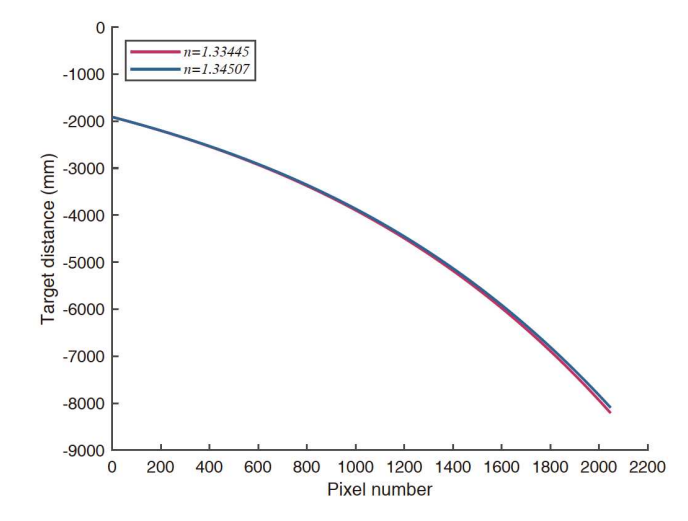
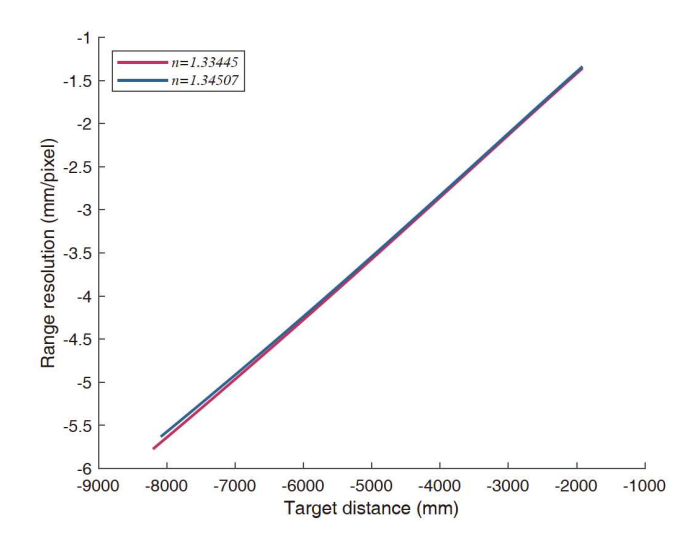


Figure 9 (Color online) Relationship between the target distance and the distance resolution. The solid red line in the graph represents the relationship curve between the target distance and the distance resolution calculated by the theoretical model. The blue dots in the figure represent the object space distance corresponding to each pixel calculated from the 50 mm step captured in the experiment, representing the distance resolution measurement value. It can be seen that the experimental results are basically consistent with the theoretical curve, which verifies the correctness of the theoretical resolution calculation model.



**Figure 10** (Color online) Relationship between pixel position and distance when the refractive indices of water are 1.33445 and 1.34507. The refractive index of the red curve is 1.33445, and the refractive index of the blue curve is 1.34507.



**Figure 11** (Color online) Relationship between target distance and range resolution when the refractive indices of water are 1.33445 and 1.34507. The refractive index of the red curve is 1.33445, and the refractive index of the blue curve is 1.34507.

view and high-resolution ULSS LiDAR was designed and demonstrated. Several pool experiments were carried out, in which a millimeter-level distance resolution was achieved. Moreover, to verify the correctness of the theoretical model, the distance resolutions in different target distances were tested, and the result shows a good consistency with the theoretical model. This study can provide academic support for the design of ULSS LiDAR and improve the accuracy of underwater Scheimpglug LiDAR design.

The underwater LiDAR significantly reduces the backscattered light from the water body using light-sheet illumination and increases the baseline. It can still maintain good backscattering suppression ability without using polarization and distance gating backscatter filtering techniques and is suitable for underwater 3D target imaging.

To further increase the depth range of ULSS LiDAR, a single illumination light source, and dual camera imaging ULSS LiDAR system can be formed by adding a Scheimpflug imaging camera without reducing the underwater distance resolution. The depth range of ULSS imaging can be increased to 1.9–50 m, which can meet most underwater application needs, such as underwater terrain exploration, underwater target survey, underwater rescue, exploration of underwater cultural relics, and other fields.

**Acknowledgements** This work was supported by the Special Project of Strategic Leading Science and Technology of Chinese Academy of Sciences (Grant No. XDA22030201).

#### References

- 1 Watson J. Underwater visual inspection and measurement using optical holography. Opt Lasers Eng 1992, 16: 375–390
- 2 Ouyang B, Dalgleish F, Vuorenkoski A, et al. Visualization and image enhancement for multistatic underwater laser line scan system using image-based rendering. IEEE J Ocean Eng., 2013, 38: 566-580
- 3 Massot-Campos M, Oliver-Codina G. Optical sensors and methods for underwater 3D reconstruction. Sensors, 2015, 15: 31525–31557
- 4 Mobley C. The optical properties of water. In: Handbook of Optics. 2nd ed. New York: R.R. Donnelly & Sons Company, 1995
- 5 Reineman B D, Lenain L, Castel D, et al. A portable airborne scanning LiDAR system for ocean and coastal applications. J Atmos Ocean Tech, 2009, 26: 2626–2641
- 6 McLean E A, Burris H.~R. J, Strand M P. Short-pulse range-gated optical imaging in turbid water. Appl Opt, 1995, 34: 4343–4351
- 7 Risholm P, Thorstensen J, Thielemann J T, et al. Real-time superresolved 3D in turbid water using a fast range-gated CMOS camera. Appl Opt, 2018, 57: 3927–3937
- 8 Tan C S, Sluzek A, Seet G G. Model of gated imaging in turbid media. Opt Eng. 2005, 44: 116002
- 9 Dalgleish F R, Caimi F M, Vuorenkoski A K, et al. Experiments in bistatic laser line scan (LLS) underwater imaging. In: Proceedings of Oceans 2009. Biloxi, 2009
- 10 Dalgleish F R, Caimi F M, Britton W B, et al. An AUV-deployable pulsed laser line scan (PLLS) imaging sensor. In: Proceedings of 2010 Conference on Optical Fiber Communication (OFC/NFOEC). Vancouver, 2007. 1–5
- 11 Dalgleish F, Caimi F, Britton W, et al. Improved LLS imaging performance in scattering-dominant waters. In: Proceedings of SPIE— The International Society for Optical Engineering. 2009
- Moore K D, Jaffe J S, Ochoa B L. Development of a new underwater bathymetric laser imaging system: L-bath. J Atmos Ocean Technol, 2000, 17: 1106–1117
- 13 Gordon A. Use of laser scanning system on mobile underwater platforms. In: Proceedings of the 1992 Symposium on Autonomous Underwater Vehicle Technology. Washington, 1992. 202–205
- 14 Bodenmann A, Thornton B, Ura T. Generation of high-resolution three-dimensional reconstructions of the seafloor in color using a single camera and structured light. J Field Robot, 2017, 34: 833–851
- 15 Imaki M, Ochimizu H, Tsuji H, et al. Underwater three-dimensional imaging laser sensor with 120-deg wide-scanning angle using the combination of a dome lens and coaxial optics. Opt Eng. 2016, 56:

#### 031212

- 16 Marshall G, Stutz G. Synchronous laser line scanners for undersea imaging applications. In: Handbook of Optical and Laser Scanning, 2nd ed. London: CRC Press, 2011. 731–750
- 17 Klopfer F, Hammerle M, Hofle B. Assessing the potential of a low-cost 3-D sensor in shallow-water bathymetry. IEEE Geosci Remote Sens Lett. 2017. 14: 1388–1392
- 18 Matos G, Buschinelli P, Pinto T. Underwater laser triangulation sensor model with flat refractive interfaces. IEEE J Ocean Eng, 2020, 45: 937–945
- 19 Scheimpflug T. Improved method and apparatus for the systematic alteration or distortion of plane pictures and images by means of lenses and mirrors for photography and for other purposes. GB190401196DA, 1904
- 20 Brydegaard M, Gebru A, Svanberg S. Super resolution laser radar with blinking atmospheric particles—application to interacting flying insects. Prog Electromagnet Res, 2014, 147: 141–151
- 21 Mei L, Brydegaard M. Atmospheric aerosol monitoring by an elastic Scheimpflug LiDAR system. Opt Express, 2015, 23: A1613
- 22 Mei L, Guan P, Yang Y, et al. Atmospheric extinction coefficient retrieval and validation for the single-band Mie-scattering Scheimpflug LiDAR technique. Opt Express, 2017, 25: A628
- 23 Mei L, Guan P. Development of an atmospheric polarization Scheimpflug LiDAR system based on a time-division multiplexing scheme. Opt Lett, 2017, 42: 3562
- 24 Mei L, Kong Z, Guan P. Implementation of a violet Scheimpflug LiDAR system for atmospheric aerosol studies. Opt Express, 2018, 26: A260
- 25 Malmqvist E, Brydegaard M, Aldén M, et al. Scheimpflug LiDAR for combustion diagnostics. Opt Express, 2018, 26: 14842–14858
- 26 Zhao G, Ljungholm M, Malmqvist E, et al. Inelastic hyperspectral LiDAR for profiling aquatic ecosystems. Laser Photon Rev, 2016, 10: 807–813
- 27 Mei L, Brydegaard M. Continuous-wave differential absorption Li-DAR. Laser Photon Rev, 2015, 9: 629–636
- Zhang Y, Zhang H, Wu S. Design of water Scheimpflug LiDAR technology used for measuring small angle backscattering. Acta Opt Sin, 2020, 40: 1101004
- 29 Liu Z, Che H, Gong Z, et al. Development of Scheimpflug LiDAR technique for measuring attenuation coefficient of water body. Chin J Laser, 2022, 49: 1210003
- 30 Gao F, Lin H, Chen K, et al. Light-sheet based two-dimensional Scheimpflug LiDAR system for profile measurements. Opt Express, 2018, 26: 27179
- 31 Chen K, Gao F, Chen X, et al. Overwater light-sheet Scheimpflug LiDAR system for an underwater three-dimensional profile bathymetry. Appl Opt, 2019, 58: 7643
- 32 Lyu N, Yu H, Han J, et al. Structured light-based underwater 3-D reconstruction techniques: A comparative study. Opt Lasers Eng, 2023, 161: 107344
- 33 Wang X, Fan J, Deng S, et al. An underwater structured light vision calibration method considering unknown refractive index based on Aquila optimizer. IEEE Trans Instrum Meas, 2023, 72: 1–12
- 34 Xu L, Zhou Y, Zhao X. A multi-refraction-based 3D reconstruction method for underwater measurement with rotating scanning. J Modern Opt, 2023, 70: 1–14
- 35 Li X, Chen X, Li W, et al. High-accuracy calibration method for an underwater one-mirror galvanometric laser scanner. Opt Express, 2023, 31: 5973–5989
- 36 Malacara D, Malacara Z, Malacara D. Handbook of Optical Design. In: Optical Engineering. 2nd ed. New York: Marcel Dekker, 2004
- 37 Austin R W, Halikas G. The index of refraction of seawater. UC San Diego: Scripps Institution of Oceanography, 1976